Solidification in Direct Metal Deposition by LENS Processing

William Hofmeister, Michelle Griffith, Mark Ensz, John Smugeresky

Thermal imaging and metallographic analysis were used to study Laser Engineered Net Shaping (LENS™) processing of 316 stainless steel and H13 tool steel. The cooling rates at the solid-liquid interface were measured over a range of conduction conditions. The length scale of the molten zone controls cooling rates during solidification in direct metal deposition. In LENS processing, the molten zone ranges from 0.5 mm in length to 1.5 mm, resulting in cooling rates at the solid-liquid interface ranging from 200–6,000 Ks⁻¹.

INTRODUCTION

The flexible fabrication of metallic objects by direct metal deposition holds considerable promise for prototype fabrication and repair. Laser Engineered Net Shaping (LENS™), being developed at Sandia National Laboratories as a co-operative R&D agreement involving government agencies, industrial participants, and university researchers, has potential for complex prototype fabrication, small lot production, precision repair or feature addition, and tooling.[1–4] The real promise of the technology, however, is to manipulate material fabrica-

tion and properties by precision deposition of the material using thermal behavior control, layered or graded deposition of multi-materials, and process parameter selection.[5–10]

Parts have been fabricated by LENS processing from numerous materials, including stainless steels (304L, 316, 17-4), nickel-based alloys (INCO designations 718, 625, 600, and 690), tool steel (H13), and titanium (alloy Ti-6Al-4V). The resultant mechanical properties confirm this process as a viable method for fabricating structural materials. The key to the mechanical strength of materials in the as deposited condition is the solidification microstructure. Quench rates for the LENS process are sufficiently fast to reduce segregation and provide a microstructural scale consistent with rapid solidification microstructures.

This article examines deposits of 316 stainless steel (316SS) and H13 tool steel (H13) in thin, single-pass wall-builds as a function of laser power, traverse velocity, and height. Thermal images of the melt pool were obtained for these experiments, and the gradients and cooling rates along the trailing edge of the melt pool were evaluated. Cooling rates at the solid-liquid interface ranged from 10^2 to 10^3 Ks⁻¹. Considering the size scale of the molten pool (~1 mm), the cooling rates in these experiments are consistent with other metal-solidification techniques. The LENS microstructural scale falls between arc-welding processes and atomization processes. This additive process is unique because parts of considerable size (centimeter to meter length scales) can be fabricated with microstructures more characteristic of rapid solidification. Thermal imaging can be used to control cooling rates during deposition to enable better microstructural control over a wide range of part geometries.

HEAT TRANSFER

In simplest terms, the heat transfer in LENS can be modeled by considering the heat transfer to the molten pool of material. The rate of heat transfer to the pool per-unit time ($\dot{q}_{in}$) is:

$$\dot{q}_{in} = \alpha_\lambda \, Q_{laser} \qquad (1)$$

where α_λ is the absorptivity at the laser wavelength, and Q_{laser} is the laser power in watts (W). The heat loss to the sur-
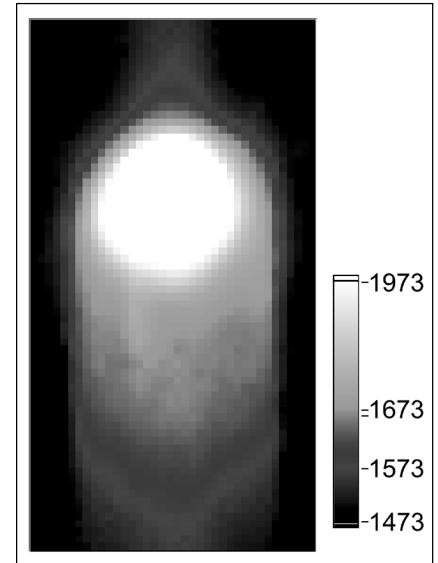

Figure 2. A thermal image of a 316 stainless steel thin wall build. Temperatures are in Kelvin. The alloy liquidus is 1,673 K.

roundings ($\dot{q}_s$) is:

$$\dot{q}_s = \kappa \vec{\nabla} T - hA(T - T_0) - \varepsilon A \sigma (T^4 - T_0^4) - \rho V$$

$$\left(\int_{T_0}^{T_m} c_s \, dT + \Delta H_f + \int_{T_m}^{T} c_l \, dT \right) \qquad (2)$$

where κ is the thermal conductivity, T is the temperature of the molten pool, T_o is the temperature of the surroundings, h is the convective heat-transfer coefficient, ε is the total hemispherical emissivity, A is the surface area of the pool, σ is the Stephan-Boltzmann constant, ρ is the density, V is the volume of the added material, c_s and c_l are the specific heats of solid and liquid material, T_m is the melting temperature, and ΔH_f is the specific heat of fusion. Typical build conditions for LENS 316SS are 0.5 mm layers at 0.5 mm spacing at a traverse velocity of 8.47 mm s⁻¹ at a laser power of 360 watts. The net rate of material deposition is 2.2 mm³ s⁻¹, so that for a stainless steel alloy the fourth term in the right hand side of Equation 2 is about 5 W. The pool volume, which is dependent on the laser power, velocity, and conduction path, has a typical value of approximately 0.5 mm³. Considering the radiation of a hemispherical cap the size of the molten pool with a 300 K superheat gives 0.6 W
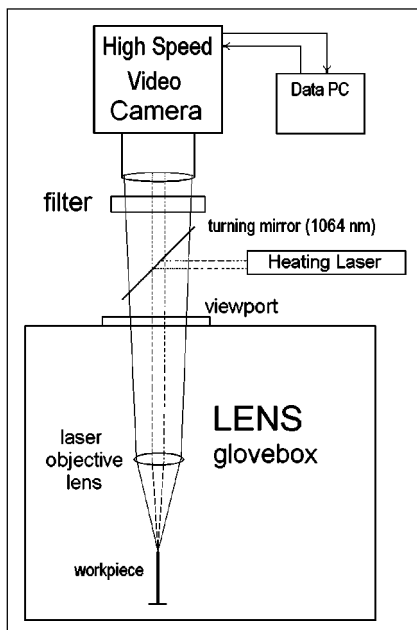

Figure 1. The position of the thermal imaging camera in relation to the laser and molten pool is shown in this schematic of the experimental setup.

for the third term on the right-hand side of the equation. The process gas is argon, and the approximate gas-flow velocity at the powder nozzle is typically 30 ms^{-1}. For this flow rate, the Reynolds number for the length scale of the molten pool is of the order 10^3 and the upper bound convective heat-transfer coefficient of the order 10^3 Wm^{-2}K^{-1}. The estimated convective heat loss is then about 2.5 watts. The absorptivity of 316SS is 0.35, so that the heat in from Equation 1 is 126 W for this example. One can see from this approximation that 4% of the energy is used to heat and melt new material and more than 90% of the heat is conducted through the substrate. Therefore, heat carried out of the molten pool is dominated by the first term on the right hand side of Equation 2. The geometry and temperature of the substrate are the most important factors in determining molten-pool size at a given input power and traverse velocity.

THERMAL IMAGING

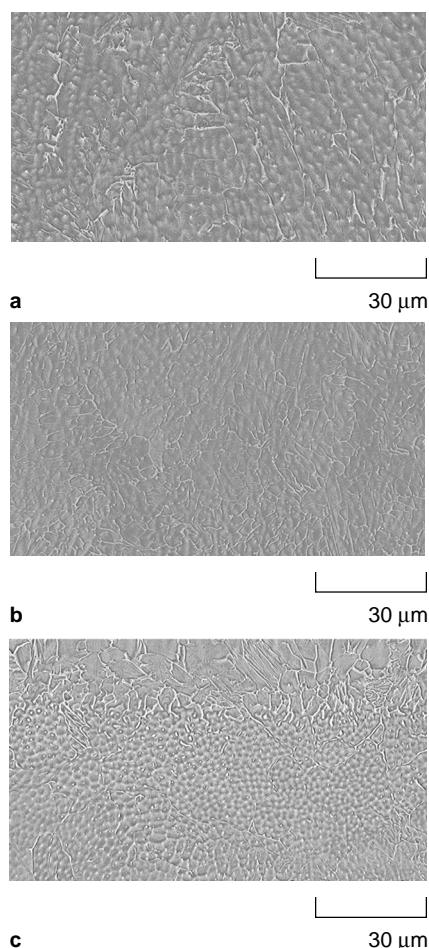In this work, thermal imaging was used to measure the temperatures, gra-

a   30 µm

b   30 µm

c   30 µm

Figure 3. The microstructures of 316SS: (a) is from the top (z = 20 mm) of the 478 W, 5.93 mm/s build, (b) is from the bottom (z = 2 mm) of the 365 W, 7.62 mm/s build, and (c) is from the bottom (z = 1 mm) of the 212 W 9.31 mm/s build. The microstructure is austenite with intercellular ferrite. (etchant: glyceriga).

a   30 µm

b   10 µm

c   30 µm

d   10 µm
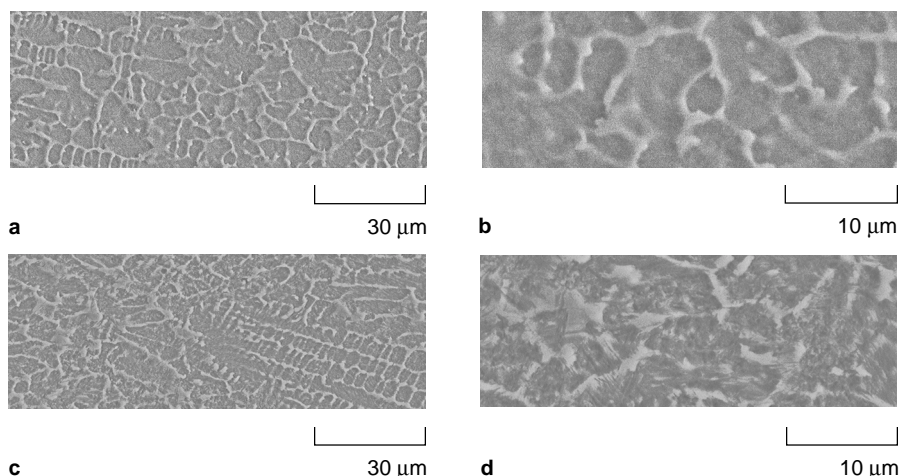
Figure 4. The microstructures of an H13 build, processed at 403 W and 7.62 mm/s: (a) and (b) are at z = 20 mm from the substrate, (c) and (d) are at z = 2 mm from the substrate. Because the lower layers are subjected to more re-heating from subsequent passes, more tempering is evident. (etchant: Villella's).

dients, and cooling rates around the melt pool. Thermal imaging is achieved by simple radiation pyrometry, where each pixel in an array is calibrated for temperature measurement. A 12-bit digital charge-couple device (CCD) camera was used to measure the radiant intensity from the sample at 650 nm through the laser-focusing objective. This wavelength is sufficiently removed from the laser wavelength (1,064 nm) that the laser light does not interfere with the measurements. The camera and optical elements were calibrated with a tungsten strip lamp.[11] Images were acquired by a National Instruments frame grabber at 490 frames per second. The temperature corresponding to each pixel in the array was calculated using standard pyrometric techniques.[12] A schematic of the experimental setup is shown in Figure 1. The advantage of this experimental setup is that the imager is stationary and has the same focal point as the laser. The work-piece is moved by x and y stages under the laser beam, and the height of the build is adjusted by moving the laser objective. The imager is always in focus and viewing the molten pool regardless of the x, y, and z positions. A temperature map of the deposition melt pool (in-situ snapshot) on a thin wall build is shown in Figure 2. The liquidus of the alloy is reported as 1,673 K and the solidus as 1,645 K.[13] The image is a thermal map of the top surface of the build. From this data it is possible to find the super-heat, liquidus, and solidus isotherms, and calculate the gradient in temperature in and around the molten pool.

MATRIX OF EXPERIMENTS

In order to better understand the range of cooling rates available to LENS processing, a simple matrix of experiments was designed around the nominal operating conditions. Each material was processed at three laser powers and three traverse velocities. For 316SS, 212 W, 365 W, and 478 W were used at 5.93 mm/s, 7.62 mm/s, and 9.31 mm/s. For H13 tool steel, the same traverse velocities were used but at 308 W, 403 W, and 498 W laser power. Single-pass walls were built at each of the nine settings, and thermal images were recorded as a function of z height (i.e., layer number). Single-pass walls change conduction conditions on each layer. As z height increases, each deposited layer is farther from the substrate, and each layer is deposited on increasingly warmer material farther from the heat sink of the substrate. Heat conduction is greatest for the first layer, where the pass is deposited onto a cold substrate, and consequently, the first layer has the smallest molten pool at constant velocity and power. This matrix of experiments gives a full range of conduction conditions encountered in building parts, and the resulting molten-pool sizes for each value of laser power and traverse velocity.
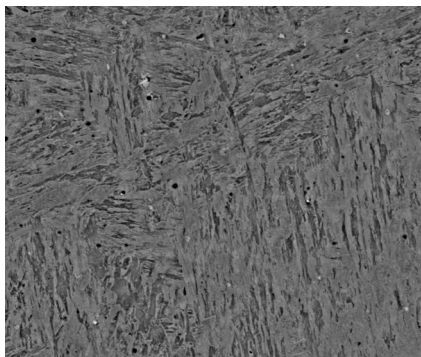
MICROSTRUCTURE

As with any rapid solidification or welding process, the microstructure in any local section of the sample contains a variation in length scales. The travel velocities are small compared to the kinetic limitations of growth, and solidification should follow the heat-flow direction resulting in a variety of growth directions and crystal orientations. The thermal gradients in the LENS process drive Marangoni convection, and solidification is not a steady-state process. In addition, considerable re-melting and coarsening occurs subsequent to the initial deposition. Since dendritic features were not well preserved, the mean intercept length between cells was chosen as a measure of the microstructural length scale, and measured in each of the build conditions. The change in this scale was not pronounced over the range of build

conditions for either 316SS or H13. In the 316SS samples the average intercept length at the bottom of the build, where conductive cooling was highest, was 4.5 μm. The overall range was from 4.2–4.8 μm. Above the base plate (>4 mm) the average was 5.4 μm with a range of 5.1–5.7 μm. In the H13 steel, at the bottom the mean intercept, length was 5.7 μm with a range of 4.8–6.4 μm, and near the top (z = 20 mm) the average was 7.4 μm with a range of 7.1–7.7 μm. In general, the microstructural scale was more sensitive to variations in z height than to changes in laser power and traverse velocity, as anticipated by Equation 2. The changes in the conduction condition, thus, have a greater effect on cooling rate and structure than the laser power and traverse velocity, as discussed earlier.

Typical 316SS microstructures from three build conditions are shown in Figure 3. The sample in Figure 3a is from the top of the 478 W, 5.93 mm/s build, and shows more ferrite than the other microstructures. Figure 3c is at the fastest speed and lowest power, and shows a portion of the subsequent pass shown at the top of the micrograph. The contrast of length scales in this single micrograph is typical of LENS deposits. The morphology is primary austenite cells with intercellular ferrite. Austenite is the primary phase formed in the solidification process, and

a   50 μm
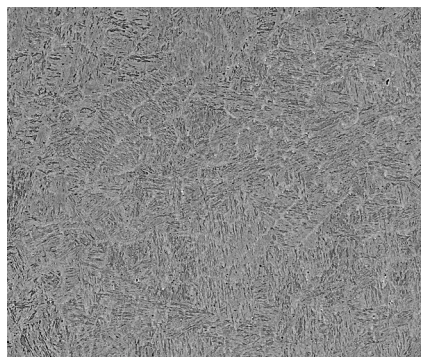
b   10 μm

Figure 5. Two microstructures of H13 builds are shown. These samples have been double tempered for two hours at 593°C.
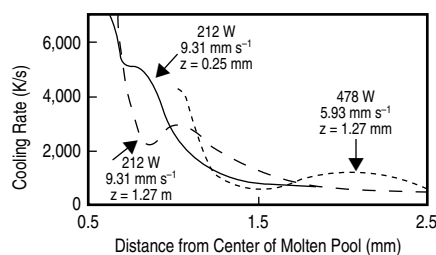
Figure 6. The cooling rates along the axis of the 316SS thin wall builds as a function of distance from the center of the molten pool are shown. Two curves were taken from the 212 W, 9.31 mm/s data and one from the 478 W, 5.93 mm/s data.

rejection of solute at the solidifying interface enriches the intercellular areas in chromium and molybdenum. According to the Schaeffler diagram for stainless-steel weld meta,[14] the Ni/Cr equivalent ratios (~1 for 316SS) are such that austenite should form exclusively. The ferrite formed from LENS processing, measured metallographically, was 3–10 volume percent of the microstructure for samples in the matrix of experiments.

Typical H13 microstructures are shown in Figure 4. While the overall length scale of the microstructure changes little (Figure 4a and 4c, respectively), the amount of tempering from subsequent laser passes is much greater at the bottom (Figure 4d) than at the top of the build (Figure 4b). At the top of the build, the material solidifies as a high-carbon austenite with intercellular ferrite. Energy-dispersive spectroscopy was used to measure the concentrations of alloying elements in the cellular and intercellular regions. The intercellular regions were rich in chromium, molybdenum, and vanadium. The rejection of these elements at the solidifying interface of the austenite phase stabilizes the ferritic intercellular regions. Some austenite is retained at the top of the builds. The retained austenite transforms to martensite and is tempered on subsequent laser passes. Although the intercellular ferrite is partially transformed to martensite, as seen in Figure 4d, a significant amount of ferrite remains. This ferritic phase is not highly segregated, however, and the retained ferrite can be transformed to martensite by tempering. Figure 5 shows LENS samples that have been double tempered at 593°C for two hours. These microstructures are nearly devoid of the ferritic phase, showing that, in these thin samples, full annealing

in the austenite region is not required to obtain fully tempered martensitic structures in H13.

TEMPERATURE AND GRADIENT PROFILES

The thermal images can be evaluated to locate the solidus and liquidus isotherms around the molten pool. The smallest molten pool and solidus area occurred on the first pass at the highest velocity and lowest power. The largest melt pool and solidus areas were found at passes sufficiently away from the substrate at the highest power and lowest travel velocity in the matrix of experiments. As the laser energy ($\alpha_\lambda Q/v$) increases, the molten pool grows in x and y. The separation of the solidus and liquidus isotherms behind the laser beam also increases with $\alpha_\lambda Q/v$.

Temperature along the axis of the wall builds and can be extracted from the thermal images. If these temperature curves are differentiated in the direction of travel, the temperature gradients are obtained along the traverse direction, which can be translated to cooling rates in the direction of travel by dividing by the traverse velocity. Three of the cooling-rate curves are shown in Figure 6. These gradient curves are distinct in that there is a local minimum in cooling rate behind the molten pool. This minimum is due to the release of the latent heat of fusion at the solidifying interface. The first local minimum, therefore, defines the dimensions of the molten zone. Furthermore, the temperature at which this minimum occurs is a measure of the temperature at the solid-liquid interface. From these images can be obtained the dimensions of the molten pool as well as some measure of the cooling rate and temperature at the growing interface. At high power, low traverse velocity, and low conductive-heat transfer (z height >
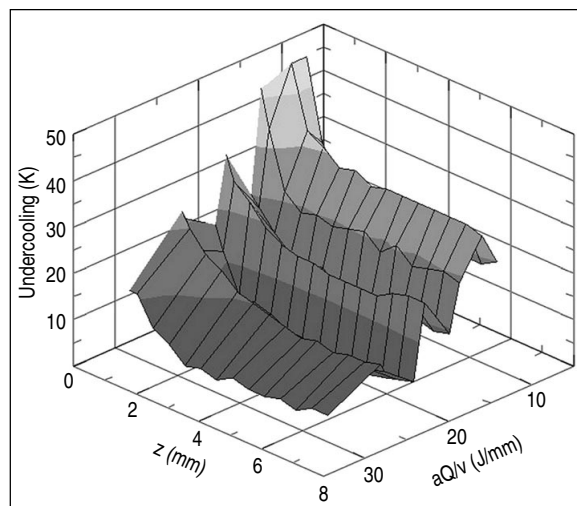
Figure 7. The undercooling at the first local minimum after the melt pool is shown for the 316SS matrix of experiments as a function of laser energy and z height.
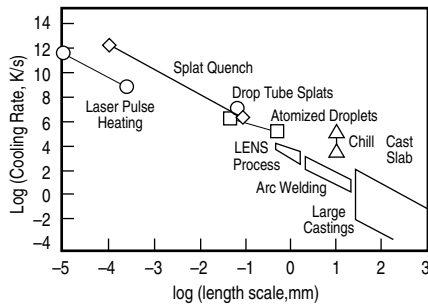
Figure 8. Cooling rates for metallic material process are plotted with length scales. Laser pulse heating of copper,[17] splat quenching of iron on a copper substrate,[20] drop-tube splats,[21] and chill-cast slab[23] use the length scale of thickness. Atomized droplets[24] use the diameter. Arc welding[25] and large castings[21] use volume to surface area. The LENS processing (this study) scale is the length of the melt pool.

3 mm), the interface temperature approaches the liquidus and the cooling rates at the solid-liquid interface are of the order 10^2 Ks^{-1}. At low power, high traverse velocities, and close to the substrate (low z height), cooling rates at the interface are 10^3 Ks^{-1}. For the latter high quench rates, the interface temperature is suppressed below the liquidus, and undercooling at the solid-liquid interface is observed. A three-dimensional (3-D) plot of the undercooling observed in the matrix of 316SS experiments is shown as a function of z height and laser energy ($\alpha_\lambda Q/v$) in Figure 7. The reported freezing range of this alloy is 28K,[13] so that the interface temperature spans a range from the liquidus to just below the solidus in these experiments.

COOLING RATES IN SOLIDIFICATION

An analysis of cooling rates in LENS processing naturally begins with the Rosenthal[15] solution for a traveling point source in a semi-infinite medium. In the 3-D solution, the cooling rates of the Rosenthall solution should scale with the traverse velocity,[16] where:

$$\frac{\partial T}{\partial t} \propto \frac{\kappa v}{\alpha_\lambda Q_{laser}} (T - T_0)^2 \qquad (3)$$

In real part fabrication, however, the medium is finite and steady-state gradients are rare. The matrix of thin wall builds described in this work allows a quasi steady-state gradient in the middle of each pass, which more closely approximates a two-dimensional situation. In many cases, LENS processing is closer to a transient laser heating condition. A zero order approximation of cooling rate for transient cases can be derived from Bloemburgen.[17] In this approach, heat from a laser pulse is compared to the thermal diffusion length of the conducting material. In metals, the optical absorption depth is small compared to the

thermal diffusion length, so the temperature rise, ΔT, for a laser pulse of duration t_p is:

$$\frac{\Delta T}{t_p} = \frac{\alpha_\lambda I}{\rho c (2\alpha_t t_p)^{1/2}} \qquad (4)$$

where I is the laser fluence in Wcm^{-2}, and α_t is the thermal diffusivity. To scale the problem to traverse velocity, the beam diameter (d) divided by the traverse velocity, dv^{-1}, is substituted for t_p, arriving at:

$$\frac{\Delta T}{\Delta t} = \frac{\alpha_\lambda Q_{laser} v^{1/2}}{d^2 (2\rho c \kappa d)^{1/2}} \qquad (5)$$

to describe the cooling rate for transient laser heating. Here, the cooling rate increases with the laser power increases, opposite to the result obtained by Rosenthal. In Equation 5, the cooling rate is proportional to the square root of traverse velocity and inversely proportional to the square root of thermal conductivity. In studies of laser heat treatment, Kear[18] noted that the cooling rate increased with laser power. In these situations, as well as in splat cooling, quenching occurs by conduction of heat through the substrate, and cooling is limited (on the upper bound) by the theoretical maximum conduction through the substrate.

These two analytical solutions give quite different results for the effects of laser power, traverse velocity, and thermal conductivity on the cooling rate. Clearly, 3-D modeling techniques (such as finite element analysis),[19] which can handle transient heating and material addition, are required to predict the cooling rates during deposition. For microstructural and dimensional control, it is desirable to program laser power and traverse velocity in the build process to keep the desired cooling rate at any point in the build, regardless of the conduction path and substrate temperature. Currently, the conduction path and temperature of the substrate are not known with enough certainty to calculate the cooling rates and pre-program the proper
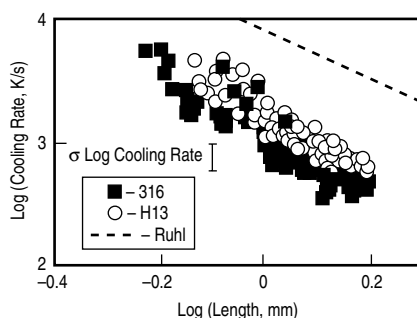

Figure 9. The measured cooling rates at the first local minimum behind the melt pool are plotted versus the project melt pool length for 316SS and H13. Ruhl's prediction[20] for a nickel splat on a copper substrate is included for comparison. The error bar is a typical one-sigma deviation of the cooling rate measurements for each experiment.

laser power and velocity to proscribed cooling rates. (The previous discussion noted that this conduction path accounts for 90% of the heat removal from the melt pool.) While finite element modeling and other methods may make this problem tractable, there is no direct way to connect the build process to the cooling rate at the solid-liquid interface.

In solidification processes, the freezing rate (the inverse of cooling rate) is proportional to the length scale of the molten zone. From the early work of Neumann,[20] the freezing rate was found to be proportional to the square root of thickness. Chvorinov[21] extended this analysis to metal castings, where the freezing time was found to be proportional to (volume/area)^2 (see also Adams[22]). This is not surprising, given that Fourier number ($\alpha_t t/L^2$) is the common non-dimensional quantity used in conduction heat-transfer solutions. A number of analyses of cooling rates for various length scales are plotted in Figure 8. Generally, the slope of the processing envelope is –2, reflecting the dependence of cooling rate on the inverse square of the length scale of the molten zone. The LENS process approaches rapid solidification at high travel speeds on cold substrates. As the size of the molten zone increases, cooling rates are equivalent to arc welding processes.

An empirical scaling approach is presented here that follows the reasoning of Figure 8. The balance of heat into and out of the molten pool in a quasi steady-state situation results in a molten zone with a length scale characteristic of the conduction heat-flow conditions. The square of this length scale should be inversely proportional to the cooling rate. The log of the cooling rate at the solid-liquid interface for the matrix of experiments is plotted vs. the log of the length of the melt pool in Figure 8 for 316SS and H13. The prediction from Ruhl[20] for splat quenched nickel on a copper substrate is included for comparison. The points in these graphs (128 for each material) represent the molten-pool length and cooling rate for every experiment in each matrix. These data points cover the entire range of laser powers, traverse velocities, and heights above the substrate in the matrix of experiments. This data fits the form:

$$\log \dot{T} = a \times \log(\text{pool length}) + b \qquad (6)$$

over the entire range of tested conditions. The slope, a, is –2.02 for 316SS and –2.18 for H13, and the intercepts, b, are 3.0 and 3.1, respectively. It is clear from this representation that the length of the molten zone is an appropriate length scale for LENS processing, since this scale obeys the conduction cooling relationship of Figure 8. Regardless of the power, traverse velocity, and conduction path,

the square of length of the molten pool largely determines the cooling rate.

In these single-pass experiments, measurement of the cooling rate is relatively straightforward in that the direction of travel is known and constant on a layer. The images can be averaged to determine the temperature profiles and gradients. In a normal build, the direction of travel changes frequently and the beam travel vector information is difficult to extract. Because of this and the difficulty in measuring the derivative of temperature from real time data, it is impractical to measure cooling rates with the thermal imaging system in real time. The scaling of Figures 8 and 9, however, suggest that cooling rate can be approximated by knowing the length of the molten pool. The thermal imager can measure the length of the molten pool without knowledge of the direction of travel. The molten pool length can be increased or decreased by modulating laser power. Consequently, based on a simple measurement of melt-pool length, the laser power can be controlled in real time to achieve a desired molten pool length and, hence, the cooling rate and solidification structure.

ACKNOWLEDGEMENTS

References

1. M.L. Griffith et al., "Free Form Fabrication of Metallic Components Using Laser Engineered Net Shaping (LENS™)," *Proc. of the Solid Freeform Fabrication Symp.*, (Austin, TX: The University of Texas at Austin), p. 125.
2. Dave M. Keicher and John M. Smugeresky, "The Laser Forming of Metallic Components Using Particulate Materials," *JOM*, 49 (5) (1997), p. 51.
3. C.L. Atwood et al., "Laser Engineered Net Shaping (LENS™): A Tool for Direct Fabrication of Metal Parts," *Proc. Of ICALEO '98*, (Orlando, Fl: Laser Institute of America, 1999), p. E-1.
4. E. Schlienger et al., "Near Net Shape Production of Metal Components Using LENS™," *Proc. of the Third Pacific Rim International Conference on Advanced Materials and Processing*, (Warrendale PA: TMS, 1998), p. 1581.
5. M.L. Griffith et al., "Understanding Thermal Behavior in the LENS™ Process," *J. Materials Design*, 20 (2/3) (June 1999), pp. 107–114.
6. A. Vasinonta, J.L. Beuth, and M.L. Griffith, "A Process Map for Consistent Build Conditions in the Solid Freeform Fabrication of Thin-Walled Structures," in press.
7. M.L. Griffith et al., "Understanding the Microstructure and Properties of Components Fabricated by Laser Engineered Net Shaping (LENS™)," *Mat. Res. Soc. Symp. Proc. Vol. 625*, (Warrendale, PA: MRS, 2000).
8. J.A. Brooks et al., "Microstructure and Property Optimization of LENS™ Deposited H13 Tool Steel," *Proc. of the Solid Freeform Fabrication Symp.*, (Austin TX: The University of Texas at Austin, 1999), pp. 375–382.
9. J.E. Smugeresky et al., "Laser Engineered Net Shaping (LENS™) Process: Optimization of Surface Finish and Microstructural Properties," *Proc. of the World Congress on Powder Metallurgy and Particulate Materials*, (Princeton, NJ: MPIF/APMI International, 1997), Part 21.
10. M.L. Griffith et al., "Multi-Material Processing by LENS™," *Proc. of the Solid Freeform Fabrication Symp.*, (Austin TX: The University of Texas at Austin, 1997), p. 387.
11. The thermal imager was calibrated with a secondary standard tungsten strip lamp. This lamp was calibrated by the National Institute of Standards and Technology.
12. D.P. DeWitt and G.D. Nutter, *Theory and Practice of Radiation Thermometry* (New York: John Wiley and Sons, 1988).
13. Stellite Delcrome 316 powder solidus and liquidus information was obtained from the manufacturer.
14. A.L. Schaeffler, "Constitution Diagram for Stainless-steel Weld Metal .2. Schaeffler Diagram," *Metal Progress*, 106 (1) (1974), p. 227.
15. D. Rosenthal, "The Theory of Moving Sources of Heat and its Application to Metal Treatments," *Trans. Am. Soc. Min. Engrs.*, 68 (1946), p. 849.
16. R.C. Dykhuizen and D. Dobranich, Sandia National Laboratories Internal memorandum, "Cooling Rates in the LENS Process" (2 February 1998).
17. N. Bloembergen, *AIP Conf. Proc. Number 50: Laser-Solid Interactions and Laser Processing—1978*, ed. S.D. Ferris, H.J. Leamy, and J.M. Poate (New York: Amer. Inst. of Phys., 1979), pp. 1–8.
18. B.H. Kear, E.M. Breinan, and L.E. Greenwald, *Solidification and Casting of Metals*, ed. H.A. Davies (London: The Metals Society, 1979), p. 501.
19. R.K. Chin, J.L. Beuth, and C.H. Amon, *Mechanics of Materials*, 24 (1996), p. 257; and W. Hofmeister et al., *JOM-e* (July 1999), www.tms.org/pubs/journals/JOM/9907/Hofmeister/Hofmeister-9907.html.
20. R.C. Ruhl, "Cooling Rates During Splat Quenching," *Mater. Sci. Eng.*, 1 (1967), pp. 313–320.
21. W.H. Hofmeister et al., *Solidification 1998*, ed. S. Marsh et al. (Warrendale, PA: TMS, 1998), pp. 375–387.
22. C.M. Adams, Jr., "Thermal Considerations in Freezing," *Liquid Metals and Solidification*, ed. R. Madden and B. Chalmers (Cleveland, OH: ASM, 1958), pp. 187–217.
23. S.D.E. Ramati et al., "Forging of Liquid and Partially Solid Sn-15 pct Pb and Aluminum-alloys" *Met. Trans. B*, 9B (1978), p. 279.
24. C.G. Levi and R. Mehrabian, "Heat Flow in Atomized Metal Droplets," *Met. Trans. B*, 11B (March 1980), pp. 21–27.
25. O. Grong, *Metallurgical Modeling of Welding*, second edition, (London: The Institute of Materials, 1997), p. 223.

William Hofmeister is research associate professor of materials science in the chemical engineering department of Vanderbilt University. Michelle Griffith is principal member of the technical staff of Sandia National Laboratories.

For more information, contact W. Hofmeister, Department of Chemical Engineering, Vanderbilt University; hof@vuse.vanderbilt.edu.

TMS Fall 2002 Extraction and Processing Division Meeting on
Recycling and Waste Treatment in Mineral and Metal Processing: Technical and Economic Aspects
16-20 June 2002, Luleå, Sweden

Organized by

LULEÅ
UNIVERSITY
OF TECHNOLOGY

MEFOS

TMS

The TMS Fall Extraction and Processing Division Meeting in 2002 will be organized in Luleå, Sweden, jointly between TMS, MiMeR (Minerals and Metals Recycling Research Centre) at Luleå University of Technology and MEFOS, The Foundation for Metallurgical Research. The topic of the meeting will be "Recycling and Waste Treatment in Metal and Mineral Processes: Technical and Economic Aspects". The conference will be held during 16-20 June 2002 at the Nordkalotten Hotel Conference Incentive in Luleå, Sweden.

Recycling and waste treatment is a growing area in material production as new material produced from recycled material can be produced with much lower energy consumption and lower emissions to the environment. In addition, recycling contributes to the saving of the earth's limited resources. Metals can, at least in theory, be recycled indefinitely and valuable metals, as well as metals available in large quantities, have for a long time been recycled. The share of steel produced from scrap is in many countries approaching or exceeding 50% of the total production. However, on the way from the raw material (scrap or ore) to the final recycling of consumer goods, wastes with limited possibilities for recycling are produced. Products with unfavorable combinations of materials are constructed. Corrosion and wear of the products give rise to material flows, which are not easily recovered. While the amount of produced materials is steadily increasing, the need to solve the materials recycling issues is crucial for a sustainable development.

The present meeting is focusing on practical, economic and fundamental aspects of recycling and waste treatment. Presently, over 200 abstracts have been received. In addition to oral presentations, poster sessions and an exhibition will be organized. A conference proceedings volume will be available at the meeting.

To receive the second announcement and information on registration and housing, please visit the conference web site at:
www.mefos.se/TMS.htm
or e-mail the conference secretary at:
caisa.samuelsson@km.luth.se.